Available online at www.sciencedirect.com
SCIENCE DIRECT®
Journal of Computational Physics 198 (2004) 159–177
JOURNAL OF COMPUTATIONAL PHYSICS
www.elsevier.com/locate/jcp

# A superlinearly convergent finite volume method for the incompressible Navier–Stokes equations on staggered unstructured grids

D. Vidović *,[1], A. Segal, P. Wesseling

*J.M. Burgers Center and Department of Applied Mathematical Analysis, Delft University of Technology, Delft, The Netherlands*

Received 31 May 2003; received in revised form 5 November 2003; accepted 9 January 2004
Available online 10 May 2004

**Abstract**

A method for linear reconstruction of staggered vector fields with special treatment of the divergence is presented. An upwind-biased finite volume scheme for solving the unsteady incompressible Navier–Stokes equations on staggered unstructured triangular grids that uses this reconstruction is described. The scheme is applied to three benchmark problems and is found to be superlinearly convergent in space.


*PACS:* 47.11.+j

*Keywords:* Staggered unstructured grid; Finite volume method; Incompressible flow; Navier–Stokes; Vector field reconstruction

## 1. Introduction

For numerical approximation of the incompressible Navier–Stokes equations on Cartesian grids, the classical Marker and Cell scheme of Harlow and Welch [1] is the method of choice. The reasons are absence of spurious modes, good conservation properties and the fact that artificial boundary conditions are not needed.

Several generalizations of this staggered scheme have been proposed for unstructured triangular meshes in [2–9]. All these methods are first-order accurate in space. All except [8,9] are restricted to incompressible flows.

In order to obtain higher order schemes, the velocity vector field needs to be reconstructed from staggered data with sufficient accuracy. Second order accurate upwind-biased schemes have been developed on

* Corresponding author. Tel.: +31152781692; fax: +31152787245.
*E-mail addresses:* D.Vidovic@amth.tudelft.nl, d.vidovic@ewi.tudelft.nl (D. Vidović).
[1] Supported by the Technology Foundation STW, Applied Science Division of NWO and The Technology Program of the Ministry of Economic Affairs (Project No. DWI.5552).

0021-9991/$ - see front matter 
doi:10.1016/j.jcp.2004.01.005

colocated grids using polynomial reconstruction (see for example [10]). Reconstruction from staggered data has not yet been much investigated. Polynomial reconstruction in the staggered case is found in [11], which discusses reconstruction on quadrilaterals; reconstruction on triangles is much the same.

In [11] it is noted that the system of equations for the reconstruction coefficients may become singular. Here we analyze this situation and propose a method for linear reconstruction of staggered vector fields with special treatment of the divergence. We also propose an upwind-biased scheme for the Navier–Stokes equations using a two-dimensional staggered grid with triangular cells, with better than first-order convergence. This method is based on [8,9] and on a new linear reconstruction. The grid does not need to be of Delaunay type, as required in [2–6]. It uses the incompressible pressure correction method and therefore is restricted to incompressible flows. However, we do not use the assumption of incompressibility in the spatial discretization, to allow extension of the scheme to the compressible case.

Superlinear spatial accuracy of the scheme is demonstrated in Section 6. We are not concerned with time accuracy here, so we use the first-order implicit Euler method to discretize in time.

## 2. Problem formulation

The incompressible Navier–Stokes equations are

$$\nabla \cdot \vec{m} = 0, \tag{1}$$

$$\frac{\partial m^\alpha}{\partial t} + \left(u^\beta m^\alpha\right)_{,\beta} = \sigma^{\alpha\beta}_{,\beta}, \tag{2}$$

where $m^\alpha = \rho u^\alpha$ is a momentum component and $u^\beta$ is a velocity component. The density $\rho$ is taken to be unity. Greek indices indicate coordinate directions; Latin indices will refer to faces in a computational grid. The summation convection is invoked for Greek indices. The nonlinear part

$$\left(u^\beta m^\alpha\right)_{,\beta} \tag{3}$$

is the inertia term, and $\sigma^{\alpha\beta}$ is the stress tensor, defined by

$$\sigma^{\alpha\beta} = -p\delta^{\alpha\beta} + 2\mu\left(\mathrm{e}^{\alpha\beta} - \frac{1}{3}\Delta\delta^{\alpha\beta}\right) = -p\delta^{\alpha\beta} + \tau^{\alpha\beta}, \tag{4}$$

where $p$ is the pressure, $\tau^{\alpha\beta}$ is the deviatoric stress tensor, $\delta^{\alpha\beta}$ is the Kronecker delta symbol, $\mu$ is the dynamic viscosity coefficient, $\mathrm{e}^{\alpha\beta}$ is the rate of strain tensor defined by

$$\mathrm{e}^{\alpha\beta} = \frac{1}{2}\left(u^\alpha_{,\beta} + u^\beta_{,\alpha}\right), \tag{5}$$

and $\Delta$ is the divergence of the velocity, i.e.

$$\Delta = \mathrm{e}^{\alpha\alpha} = u^\alpha_{,\alpha}. \tag{6}$$

## 3. Discretization of continuity equation and staggered grids

The motivation to use a finite volume staggered scheme is to conserve the mass locally. The continuity Eq. (1) is integrated over each triangle $\Omega$ of the mesh and the divergence theorem is applied

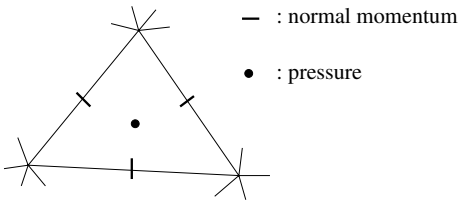


Fig. 1. Staggered positioning of the variables in an unstructured grid.

$$\int_{\Omega}(\nabla\cdot\vec{m})\mathrm{d}\Omega=\oint_{\partial\Omega}(\vec{m}\cdot\vec{n})\mathrm{d}\Gamma=0, \tag{7}$$

where $\vec{n}$ is the outward normal. Local mass conservation means that this equation should be satisfied exactly. Therefore we choose the averaged normal momentum components

$$m_e=\frac{1}{l_e}\int_{l_e}(\vec{m}\cdot\vec{N}_e)\mathrm{d}l \tag{8}$$

as our primary momentum unknowns, where $\vec{N}_e$ is one of the two possible unit normal vectors in edge $e$. Eq. (7) becomes

$$\sum_{e=1}^{3}m_e\bar{l}_e=0, \tag{9}$$

where $\bar{l}_e=(\vec{N}_e\cdot\vec{n}_e)l_e$, $\vec{n}_e$ is the outward normal in face $e$, and $l_e$ is the length of face $e$.

Pressure unknowns are associated with cells, as shown in Fig. 1.

## 4. Linear reconstruction of staggered vector fields

The scheme developed in [8,9] uses a piecewise constant reconstruction and it is therefore at most first-order accurate. In order to achieve a higher order accuracy, we shall use a linear reconstruction. Such reconstruction of staggered vector fields has been discussed in [11] for the quadrilateral case. We will discuss the triangular case.

To approximate a vector field $\vec{m}$ in the vicinity of a mesh node 0, we postulate a piecewise linear approximation of the following form:

$$\vec{m}(\vec{r})\approx\vec{P}(\vec{r})=\vec{a}+\vec{b}x+\vec{c}y, \tag{10}$$

where $\vec{r}=[x\ y]^{\mathrm{T}}$ is a position vector of a point where $\vec{m}$ is to be reconstructed, relative to node 0. We want to determine $\vec{a}$, $\vec{b}$ and $\vec{c}$ such that the face average of $\vec{N}_e\cdot\vec{P}(\vec{r})$ matches the normal component $m_e$ for face $e$ belonging to a certain set (that will be called the reconstruction stencil) as closely as possible. Fig. 2 shows a possible reconstruction stencil. This leads to the following linear system:

$$\vec{N}_e\cdot\vec{P}(\vec{r}_e)=m_e\quad\text{for each } e \text{ in the reconstruction stencil.} \tag{11}$$

This system can be written as

$$Mc=m, \tag{12}$$

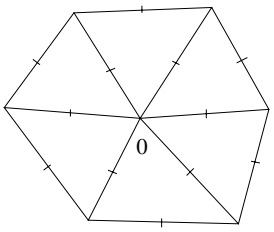


Fig. 2. Possible reconstruction stencil.

where

$$M = \begin{bmatrix} N_1^x & N_1^y & N_1^x x_1 & N_1^x y_1 & N_1^y x_1 & N_1^y y_1 \\ \vdots & \vdots & \vdots & \vdots & \vdots & \vdots \\ N_k^x & N_k^y & N_k^x x_k & N_k^x y_k & N_k^y x_k & N_k^y y_k \end{bmatrix}, \tag{13}$$

$$c = [\, a_1 \quad a_2 \quad b_1 \quad b_2 \quad c_1 \quad c_2 \,]^{\mathrm{T}}, \quad m = [\, m_1 \quad \ldots \quad m_k \,]^{\mathrm{T}}, \tag{14}$$

and $k$ is the number of faces in the reconstruction stencil.

If the tangential momentum component $m_e^{\mathrm{t}}$ is prescribed as a boundary condition in some of the boundary faces belonging to the reconstruction stencil and meeting in the central node, then the equation

$$\vec{T}_e \cdot \vec{P}(\vec{r}_e) = m_e^{\mathrm{t}} \tag{15}$$

is added to system (11) where $\vec{T}_e = (-N_e^y, N_e^x)$ and $m_e^{\mathrm{t}} = \vec{T}_e \cdot \vec{m}_e$.

In order to determine the least squares solution for $c$ it is necessary that $\mathrm{rank}(\mathrm{M}) = 6$. If $\mathrm{rank}(\mathrm{M}) < 6$, the stencil needs to be enlarged, or the degree of $P$ must be lowered. We will pursue the first option only. On general unstructured grids it is difficult to specify a priori reconstruction stencils such that $\mathrm{rank}(\mathrm{M}) = 6$. However, we can say the following: one triangle in the stencil suffices to determine $\nabla \cdot \vec{m} = b_1 + c_2$ because

$$b_1 + c_2 = \frac{1}{|\Omega|} \oint_{\partial\Omega} \vec{n} \cdot \vec{P}(\vec{r}) \mathrm{d}\Gamma = \frac{1}{|\Omega|} \sum_{e=1}^{3} \vec{N}_e \cdot \vec{P}(\vec{r}_e) \overline{l}_e. \tag{16}$$

Therefore

$$\mathrm{rank}(\mathrm{M}) \leqslant k - \tilde{k} + 1, \tag{17}$$

where $\tilde{k}$ is the number of triangles in the reconstruction stencil. Hence, for the stencil in Fig. 3 we have $\mathrm{rank}(\mathrm{M}) \leqslant 5$, so this stencil is too small, and additional faces must be added to the reconstruction stencil.

An additional rank reduction may occur in special situations. Fig. 4 shows a reconstruction stencil for a boundary node 0. Face centers 1, 2 and 3 are collinear, so there exist coefficients $\alpha$ and $\beta$ such that

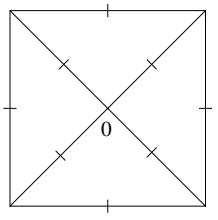


Fig. 3. Insufficient reconstruction stencil.

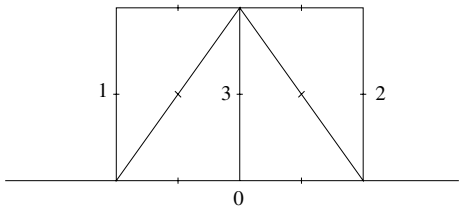


Fig. 4. Reconstruction stencil at a boundary.

$\vec{r}_3 = \alpha\vec{r}_1 + \beta\vec{r}_2$ and $\alpha + \beta = 1$. In the case presented in Fig. 4, $\alpha = \frac{1}{2}$ and $\beta = \frac{1}{2}$. These faces are also parallel, and we shall suppose that $\vec{N}_1 = \vec{N}_2 = \vec{N}_3$. By substituting this in the left hand side of the Eq. (11) for face 3 we obtain

$$\vec{N}_3 \cdot \vec{P}(\vec{r}_3) = \vec{N}_3 \cdot \vec{P}(\alpha\vec{r}_1 + \beta\vec{r}_2) = \alpha\vec{N}_1\vec{P}(\vec{r}_1) + \beta\vec{N}_2\vec{P}(\vec{r}_2). \tag{18}$$

The equation for face 3 is linearly dependent on the equations for faces 1 and 2, and $\mathrm{rank}(\mathrm{M}) \leqslant k - \tilde{k} + 1 - 1 < 6$.

If the grid is unstructured, stencils close to the stencil of Fig. 4 frequently appear at boundaries, resulting in ill-conditioned linear systems. In order to detect such situations, singular value decomposition (SVD) is used to find the pseudo-inverse of $M$. The stencil is enlarged if some singular value is less than some threshold. Because the matrices involved are small, SVD takes only a small part of total computing time.

In order to match the normal velocities in the faces closer to the center more closely than those in the outer part of the reconstruction stencil, we use weight 1 for the equations related to the faces meeting in the central node, and $10^{-2}$ for all the others. This gives practically absolute priority to the nearest neighbors, but still keeps the singular values of the reconstruction matrix relatively large. Numerical experiments have shown that two groups of singular values can be distinguished: those proportional to the larger weight, and those proportional to the smaller weight. For this reason using too small weights can have negative effect on the accuracy. On the other hand, numerical experiments also show that the momentum matrix is better conditioned if the nearest neighbors have much higher weights than the distant faces. Using ratio 1/1000 gives almost the same results. This is not a very sensitive parameter.

In order to avoid growing ill-conditioning as the mesh is refined, we scale $\vec{r}_i$ by some typical length $h$, for example the average length of the faces meeting in the central node. Hence, in (10)–(12) instead of $\vec{r}$ and $\vec{P}$ we use

$$\tilde{\vec{r}} = [\,\tilde{x} \quad \tilde{y}\,]^{\mathrm{T}} = \frac{\vec{r}}{h}, \quad \tilde{\vec{P}}(\tilde{\vec{r}}) = \vec{P}(\vec{r}) = \vec{a} + \tilde{\vec{b}}\tilde{x} + \tilde{\vec{c}}\tilde{y}, \quad \tilde{\vec{b}} = h\vec{b}, \quad \tilde{\vec{c}} = h\vec{c}. \tag{19}$$

We solve for the coefficients $\tilde{\vec{b}}$ and $\tilde{\vec{c}}$, which are used to calculate $\vec{b}$ and $\vec{c}$.

The coefficients of the linear polynomial are obtained in the form $[a_1, \ldots, c_2] = M^+ \cdot [m_1, \ldots, m_k]^{\mathrm{T}}$, where $M^+$ is the pseudo-inverse of matrix $M$. Matrix $M^+$ depends only on the grid and on the weights, and does not change in time. It can be calculated in advance and used later in each time step. This implies that a $6 \times k$ matrix must be stored for each node.

### 4.1. Divergence-free linear reconstruction

We saw that each triangle included in the reconstruction stencil imposes a condition on the divergence of the reconstruction polynomial (see (16)). Therefore it is possible to calculate the divergence $d$ of the vector field $\vec{m}$ by applying the divergence theorem on some closed curve

$$d = \frac{1}{|\Omega|}\int \nabla\cdot\vec{m}\,\mathrm{d}\Omega = \frac{1}{|\Omega|}\sum_{\alpha=1}^{k_1}\overline{l}_\alpha m_\alpha. \tag{20}$$

Since $b_1 + c_2 = \nabla\cdot\vec{P}$ in (10), we can require that $b_1 + c_2 = d$ where $d$ is calculated as in (20). Let $b_1 = d/2 + b$, $c_2 = d/2 - b$, and

$$\overline{P}_x(\vec{r}) = a_1 + bx + c_1 y, \quad \overline{P}_y(\vec{r}) = a_2 + b_2 x - by. \tag{21}$$

Note that $\nabla\cdot\overline{\vec{P}} = 0$; therefore $\overline{\vec{P}}$ will be called the divergence-free part of $\vec{P}$. The reconstruction polynomial with specified divergence $d$ can be represented in the following way:

$$\vec{P}(\vec{r}) = \overline{\vec{P}}(\vec{r}) + \frac{d}{2}\vec{r}. \tag{22}$$

The number of free parameters has dropped from six to five.

Each face $e$ in the reconstruction stencil contributes the following equation:

$$\vec{N}_e\cdot\overline{\vec{P}}(\vec{r}_e) = m_e - \frac{1}{2}(\vec{N}_e\cdot\vec{r})d. \tag{23}$$

The least squares solution is given by

$$\begin{bmatrix} a_1\\ a_2\\ b\\ c_1\\ b_2\end{bmatrix} = M^+\cdot\left(\begin{bmatrix} m_1\\ \vdots\\ m_k\end{bmatrix} - \frac{1}{2}\begin{bmatrix} N_1^x x_1 + N_1^y y_1\\ \vdots\\ N_k^x x_k + N_k^y y_k\end{bmatrix} d\right), \tag{24}$$

where $M^+$ is the pseudo-inverse of the matrix $M$ of system (23). We substitute (20) in (24) to obtain

$$\begin{bmatrix} a_1\\ a_2\\ b\\ c_1\\ b_2\end{bmatrix} = M^+\cdot\left(\begin{bmatrix} m_1\\ \vdots\\ m_k\end{bmatrix} - \frac{1}{2|\Omega|}\begin{bmatrix} N_1^x x_1 + N_1^y y_1\\ \vdots\\ N_k^x x_k + N_k^y y_k\end{bmatrix}\begin{bmatrix}\overline{l}_1 & \cdots & \overline{l}_{k_1}\end{bmatrix}\cdot\begin{bmatrix} m_1\\ \vdots\\ m_{k_1}\end{bmatrix}\right). \tag{25}$$

In this way faces used to specify the divergence $d$ enter the reconstruction stencil.

If at least five faces meet in a node, they impose enough conditions to determine the divergence-free part of a node-based linear polynomial (see Fig. 5 left and middle). However, if fewer than five faces meet in some node, the stencil is enlarged as in Fig. 5 right (or the order of interpolation must be lowered; this option we do not pursue).

Divergence-free linear reconstruction has several advantages. The most important one is that it leads to a superlinearly convergent scheme for the Navier–Stokes equations, as will be shown in the following sections, while the non-divergence-free linear reconstruction does not. In addition, it leads to a smaller stencil, and it requires roughly half the memory of the non-divergence-free reconstruction. It does not need weights, thresholds or SVD whenever at least five faces meet in a node or else tangential momentum is prescribed in a sufficient number of faces meeting in the central node. It is however not required that at least five faces meet in every internal node. Meshes that we used do not have this property.

We also tried quadratic reconstruction, which can be made divergence free as well. It does improve the accuracy, but it leads to a huge stencil, and it is also difficult to determine which thresholds and weights should be used. Quadratic reconstruction will not be further discussed here.

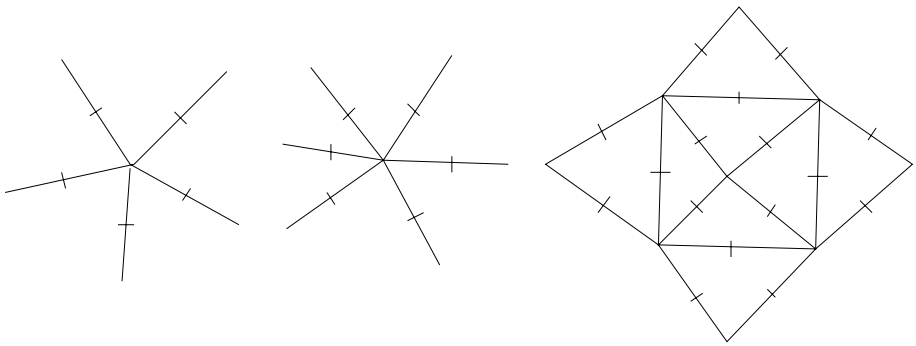

Fig. 5. Reconstruction stencils for the divergence-free node-based linear reconstruction.

## 5. Discretization of momentum equation

Eq. (2) is multiplied by $\vec{N}_i$ and integrated over the shaded control volume presented in Fig. 6, which we denote by $\Omega_i$:

$$\int_{\Omega_i} \frac{\partial(\vec{N}_i \cdot \vec{m})}{\partial t} \mathrm{d}\Omega + \int_{\Omega_i} \nabla \cdot [\vec{u}(\vec{m} \cdot \vec{N}_i)] \mathrm{d}\Omega = -\int_{\Omega_i} \vec{N}_i \cdot \nabla p \, \mathrm{d}\Omega + N_i^\alpha \int_{\Omega_i} \tau_{,\beta}^{\alpha\beta}. \tag{26}$$

### 5.1. Viscous term

We apply the divergence theorem

$$N_i^\alpha \int_{\Omega_i} \tau_{,\beta}^{\alpha\beta} \, \mathrm{d}\Omega = N_i^\alpha \oint_{\partial\Omega_i} \tau^{\alpha\beta} n^\beta \, \mathrm{d}\Gamma = N_i^\alpha \sum_e \tau_e^{\alpha\beta} N_e^\beta \overline{l}_e, \tag{27}$$

where $\tau_e^{\alpha\beta}$ is the deviatoric stress tensor averaged over the control volume face $e$, obtained as the average of the stress reconstructed in nodes 1 and 2 (see Fig. 6). The divergence for both reconstruction polynomials is calculated from the four faces that surround face $e$. Even if the flow is incompressible, the divergence should still be included when an implicit method is used, because this is found to improve the properties of the global matrix.If we use the non-divergence-free reconstruction, the local truncation error of the scheme decreases linearly as we refine the mesh, but the solution stops improving at a certain resolution. However, if the divergence-free reconstruction is used, converge does not stall and the method is superlinearly convergent, as will be demonstrated in Section 6.

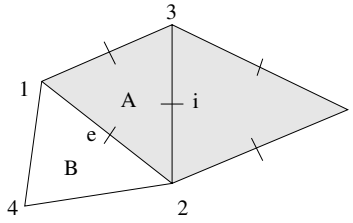


Fig. 6. Control volume for the momentum equation.

### 5.2. Inertia term

The divergence theorem gives

$$\int_{\Omega_i} \nabla \cdot [\vec{u}(\vec{m} \cdot \vec{N}_i)] \mathrm{d}\Omega = \oint_{\partial\Omega_i} (\vec{u} \cdot \vec{n})(\vec{m} \cdot \vec{N}_i) \mathrm{d}\Gamma \approx \sum_e u_e (\vec{m}_e \cdot \vec{N}_i) \bar{l}_e, \tag{28}$$

where $u_e = m_e/\rho_e$ is the average normal velocity in face $e$. Term $\vec{m}_e \cdot \vec{N}_i$ is represented as a combination of the normal and the tangential momentum in face $e$:

$$\vec{m}_e \cdot \vec{N}_i = \vec{N}_i \cdot \left( (\vec{N}_e \cdot \vec{m}_e)\vec{N}_e + (\vec{T}_e \cdot \vec{m}_e)\vec{T}_e \right) = (\vec{N}_i \cdot \vec{N}_e) m_e + (\vec{N}_i \cdot \vec{T}_e) m_e^{\mathrm{t}}. \tag{29}$$

To reconstruct $m_e^{\mathrm{t}}$ we use the divergence free linear reconstruction based in node 3 if the flow trough face $e$ is directed from node 3 to node 4, and in node 4 otherwise (see Fig. 6). If node 3 is used, the divergence is calculated from triangle A, otherwise it is calculated from triangle $B$. Below we shall refer to the node that we choose for the center of the reconstruction as the upwind node, and to the cell from which we calculate the divergence as the upwind cell.

The upwind bias is introduced to improve the condition of the matrix and to diminish numerical wiggles. We make the following approximation:

$$m_e^{\mathrm{t}} \approx \vec{T}_e \cdot \vec{P}_{\mathrm{up}}(\vec{r}_e), \tag{30}$$

where $\vec{P}_{\mathrm{up}}$ is the reconstruction polynomial in the upwind node, and $\vec{r}_e$ is the position vector of the center of face $e$ relative to the upwind node.

It is also possible to reconstruct the full vector $\vec{m}_e$ instead of $m_e^{\mathrm{t}}$, but the scheme obtained is somewhat less accurate.

### 5.3. Pressure term

Several approximations of the pressure gradient were presented in [8]. Our experience is that the path integral method with six cells gave the best results. This method first appeared in [12] and will be presented here. It is based on the identity

$$\int_a^b \nabla p \cdot \mathrm{d}\vec{x} = p_b - p_a, \tag{31}$$

where $a$ and $b$ are two points. Therefore the following approximation makes sense:

$$(\nabla p)_{ab} \cdot (\vec{x}_b - \vec{x}_a) \approx p_b - p_a, \tag{32}$$

where $(\nabla p)_{ab}$ is the pressure gradient in some point near the center of the line connecting $a$ and $b$, and $\vec{x}_a$ and $\vec{x}_b$ are the coordinates of points $a$ and $b$ respectively. We apply this formula to three pairs of cells (see Fig. 7).

$$(\nabla p)_i \cdot (\vec{x}_2 - \vec{x}_1) \approx p_2 - p_1, \tag{33}$$

$$(\nabla p)_i \cdot (\vec{x}_3 - \vec{x}_5) \approx p_3 - p_5, \tag{34}$$

$$(\nabla p)_i \cdot (\vec{x}_4 - \vec{x}_6) \approx p_4 - p_6. \tag{35}$$

Here $p_1, \ldots, p_6$ are the pressures averaged over triangles $1, \ldots, 6$ which we use as the primary pressure variables. Using these averages instead of the pressure in circumcenters is what makes it possible to

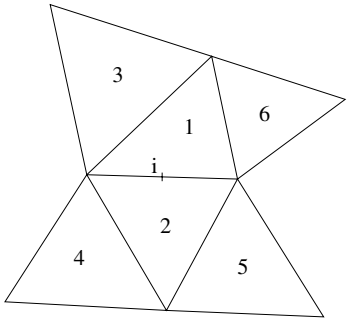


Fig. 7. Path integral method with six cells.

use non-Delaunay grids. Points $1,\ldots,6$ are the centroids of the triangles. By adding (34) and (35) we obtain

$$(\nabla p)_i \cdot (\vec{x}_3 - \vec{x}_5 + \vec{x}_4 - \vec{x}_6) \approx p_3 - p_5 + p_4 - p_6. \tag{36}$$

The pressure gradient $(\nabla p)_i$ is determined from (33) and (36).

### 5.4. Time integration

We make the following approximation:

$$\int_{\Omega_i} \frac{\partial(\vec{N}_i \cdot \vec{m})}{\partial t} \mathrm{d}\Omega \approx |\Omega_i| \frac{\mathrm{d}m_i}{\mathrm{d}t}. \tag{37}$$

Spatial discretizations of the continuity and the momentum equation presented in Sections 3 and 5 can be written as

$$Du = 0, \tag{38}$$

$$R_\mathrm{m} \frac{\mathrm{d}m}{\mathrm{d}t} + C(u)m = -R_\mathrm{m} G p + Vu, \tag{39}$$

where $m$, $u$ and $p$ are the velocity and pressure algebraic vectors of unknowns, $D$ is the discrete divergence operator, $R_\mathrm{m}$ is a diagonal matrix containing the areas of the control volumes of the discretized momentum equations, and $C$, $G$ and $V$ are the discrete convection, gradient and viscous operators, respectively.

The pressure-correction approach is used. Initial conditions determine the starting solution vectors $m^0$ and $p^{-1/2}$. In each time step $n$ first a prediction $m^*$ of the new momentum is computed as follows:

$$R_\mathrm{m} \frac{m^* - m^n}{\Delta t} + C(u^n)m^* = -R_\mathrm{m} G p^{n-1/2} + Vu^*. \tag{40}$$

Here Picard linearization is applied to the nonlinear convection term (i.e. $u$ is taken at the old time level). Next, the pressure correction $\delta p$ is computed from

$$\Delta t D G \delta p = Du^*. \tag{41}$$

Finally, the new velocity follows from:

$$u^{n+1} = u^* - \Delta t G \delta p, \tag{42}$$

and the new pressure is $p^{n+1/2} = p^{n-1/2} + \delta p$.

### 5.5. Treatment of boundaries

In each boundary face we have two boundary conditions. We may prescribe the momentum vector (for example at the inflow boundary or in the case of the no-slip condition), the normal and tangential stress (at the outflow boundary), or the normal component of one of these two and the tangential component of the other (as on free slip boundaries or at an outflow boundary).

In addition, at the outflow boundary also the pressure is given.

There is no need to integrate for faces where the normal momentum is given. For boundary faces where the normal momentum is not given a control volume consisting only of one triangle is used.

Prescribed momentum components are used in the inertia as well as in the viscous term, while the prescribed stress is used only in the viscous term.

#### 5.5.1. Inertia

If the tangential momentum $m_e^{\mathrm{t}}$ is given in some of the faces of the control volume, it is used and there is no need to reconstruct for that face. Otherwise the node belonging to the same boundary triangle as face $e$ which is opposite to this face is chosen for the upwind node.

If the upwind node falls on a boundary where the full momentum was not given, then some other node belonging to the upwind cell is chosen for the upwind node, except if they all lie on such boundaries. This improves the accuracy a bit.

#### 5.5.2. Viscosity

The term $N_i^{\alpha}\tau_e^{\alpha\beta}N_e^{\beta} = \vec{N}_i \cdot \tau_e \cdot \vec{N}_e$ needed in (27) is represented as

$$\vec{N}_i \cdot \tau_e \cdot \vec{N}_e = (\vec{N}_i \cdot \vec{N}_e)\tau_e^{nn} + (\vec{N}_i \cdot \vec{T}_e)\tau_e^{\mathrm{nt}}. \tag{43}$$

Here

$$\tau^{nn} = \vec{n} \cdot \tau \cdot \vec{n}, \quad \tau^{nt} = \vec{n} \cdot \tau \cdot \vec{t} \tag{44}$$

denote the normal and the tangential stress component, respectively, and $\vec{n}$ and $\vec{t}$ are the normal and the tangential unit vector at the boundary.

If one of the stress components is given in face $e$, it is used and only the other component is reconstructed. If $\tau^{nn}$ and $\tau^{nt}$ are given, there is no need to reconstruct.

The situation where some stress component is given in node 1 but it is not given in face $e$ (see Fig. 8) requires special care. The general rule is that one should never reconstruct the stress which is given, otherwise the scheme becomes unstable.

The deviatoric stress tensor $\tau$ is not fully determined by prescribing its normal and tangential component, because it has three degrees of freedom (see Section 2). However, we have

$$\tau^{11} + \tau^{22} = \frac{2}{3}\mu\Delta, \quad \tau^{12} = \tau^{21} \tag{45}$$

and also

$$\tau^{nn} + \tau^{tt} = \frac{2}{3}\mu\Delta, \quad \tau^{nt} = \tau^{tn}, \tag{46}$$

where $\tau^{tt} = \vec{t} \cdot \tau \cdot \vec{t}$ and $\tau^{tn} = \vec{t} \cdot \tau \cdot \vec{n}$. Furthermore,

$$\begin{bmatrix} \tau^{nn} & \tau^{nt} \\ \tau^{tn} & \tau^{tt} \end{bmatrix} = R\tau R^{-1}, \quad R = \begin{bmatrix} n^x & n^y \\ -n^y & n^x \end{bmatrix}, \tag{47}$$

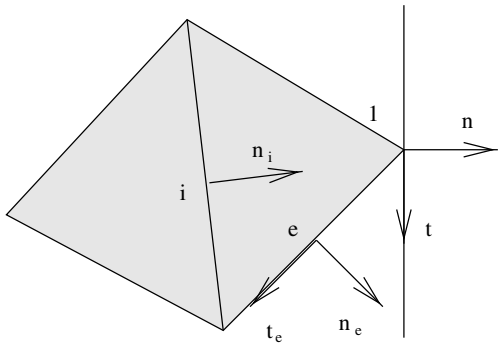


Fig. 8. Node at a boundary.

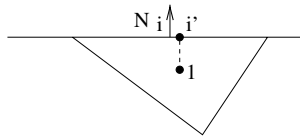


Fig. 9. Computing the pressure gradient at the outflow.

and so

$$\tau = R^{-1}\begin{bmatrix} \tau^{nn} & \tau^{nt} \\ \tau^{tn} & \tau^{tt} \end{bmatrix} R = R^{-1}\begin{bmatrix} \tau^{nn} & \tau^{nt} \\ \tau^{nt} & \frac{2}{3}\mu\Delta - \tau^{nn} \end{bmatrix} R. \tag{48}$$

If $\tau^{nn}$ and $\tau^{nt}$ are given in node 1, we obtain the divergence from the divergence theorem and use (48) to obtain the stress. Then we use it to compute $\vec{N}_i \cdot \tau_1 \cdot \vec{N}_e$. Hence there is no need for reconstruction at the outflow boundaries.

Of course, in the incompressible case one can take $\Delta = 0$. We compute the divergence implicitly.

If one stress component is given in node 1, the other is reconstructed.

*5.5.3. Pressure*

Pressure is prescribed at the outflow boundaries. The derivative of the pressure in direction $N_i$ (see Fig. 9) is computed in the following way:

$$(\nabla p \cdot \vec{N})_i = \frac{p_{i'} - p_1}{\vec{x}_{i'} - \vec{x}_1}, \tag{49}$$

where point $i'$ is the normal projection of point 1 to the boundary.

## 6. Numerical validation

### *6.1. Kovasznay flow*

This is a laminar flow behind a two-dimensional grid presented in [13] (see Fig. 10 left). The exact solution is

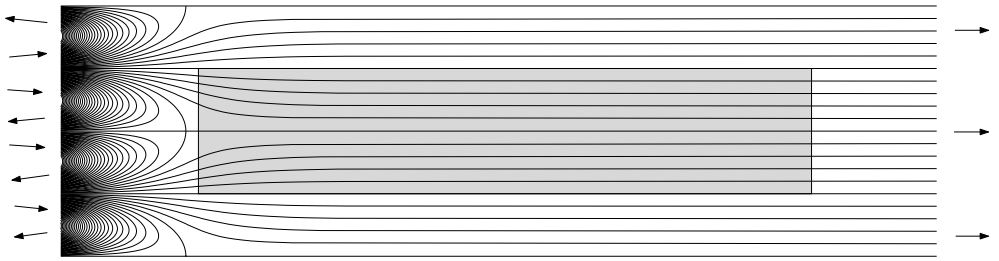

Fig. 10. Kovasznay flow – streamlines and the shaded computational domain.

$$v(x,y) = \frac{\lambda}{2\pi} e^{\lambda x} \sin(2\pi y), \quad u(x,y) = 1 - e^{\lambda x}\cos(2\pi y), \quad p(x,y) = c - \frac{1}{2} e^{2\lambda x},$$
$$\lambda = \frac{Re}{2} - \left(\frac{Re^2}{4} + 4\pi^2\right)^{\frac{1}{2}}, \tag{50}$$

where $Re = 1/\mu$.

We solved this problem for $Re = 10$ using the present method and various grids on domain $[0.1, 5] \times [-0.5, 0.5]$. The exact stress and the pressure were prescribed on the outflow boundary, and the exact velocity was prescribed on the other parts of the boundary.

The local truncation error $\tau_m$ for the momentum equation and $\tau_d$ for the continuity equation are defined as

$$\tau_m = R_m^{-1}[C(u_{ex})m_{ex} - Vu_{ex}] + Gp_{ex}, \tag{51}$$

$$\tau_d = R_d^{-1} D u_{ex}, \tag{52}$$

where $u_{ex}$ and $m_{ex}$ are the vectors of exact normal velocities and momenta averaged over the faces, $p_{ex}$ is the vector of the exact pressure averaged over the control volumes, $R_d$ is a diagonal matrix containing triangle areas, and $R_m$ is a diagonal matrix containing the areas of the control volumes for the momentum equation.

The momentum is reconstructed in each node using the divergence free linear reconstruction and the average values of the exact momentum in the surrounding faces. The vector of differences between these reconstructed momenta and the exact momenta in nodes is denoted by $\delta_m$. The vector of differences between the gradients of the reconstruction polynomials and the exact momentum gradients in nodes is denoted by $\delta_{\nabla m}$.

The (global truncation) momentum error in face $e$ is defined as

$$\varepsilon_{m,e} = m_e - m_{ex,e}, \tag{53}$$

and the (global truncation) pressure error in cell $k$ is defined as

$$\varepsilon_{p,k} = p_k - p_{ex,k}. \tag{54}$$

The $k$-norm of algebraic vector $x \in \mathbb{R}^n$ is defined as

$$\|x\|_k = \left[\frac{1}{n}\sum_{e=1}^{n} x_e^k\right]^{1/k}, \quad \|x\|_\infty = \lim_{k\to\infty} \|x\|_k. \tag{55}$$

The order of accuracy $\alpha$ is estimated in the following way. It is assumed that some norm of the error depends on $h$ as $\|\varepsilon\| \approx ah^\alpha$, $h \downarrow 0$, where $h$ is a mesh parameter (in our case, length of the faces along the leftmost boundary), $\alpha$ is the order of accuracy, and $a$ is some constant. This can be written as

$$\frac{\log a}{\log h} + \alpha = \frac{\log \|\varepsilon\|}{\log h}. \tag{56}$$

We estimate $\log a$ and $\alpha$ by least squares.

The 1-norm, 2-norm and $\infty$-norm of $\delta_{\mathrm{m}}$, $\delta_{\nabla \mathrm{m}}$, $\tau_{\mathrm{m}}$, $\varepsilon_{\mathrm{m},e}$ and $\varepsilon_{p,k}$ are shown in Figs. 11–13 as functions of a mesh parameter $h$, together with examples of the type of grid used. In order to make the tests more severe, the finer grids were not created from the coarser grids by subdividing their triangles, but were created from scratch. Unnecessarily irregular and stretched grids were used to test the scheme severely.

The accuracy of the scheme is seen to be less than second order, but convergence is clearly superlinear. As usual for schemes for the incompressible Navier–Stokes equations, pressure is approximated with less accuracy than momentum.

### 6.2. Backward facing step

The domain shown in Fig. 14 is 18.87 units long (not including the inlet) and 1 unit wide. The inlet is 0.5 units wide and 0.5 units long. The initial solution is zero. The inflow velocity profile is parabolic and given by $24t(1-y)(y-0.5)$ when $t < 1$ and $24(1-y)(y-0.5)$ for $t \geqslant 1$.

We found the stationary solution to this problem using various resolutions of two types of grid (called regular and distorted) shown in Fig. 15 for two different Reynolds numbers: 400 and 800. We define the Reynolds number as $2\rho LU/\mu$, where $L$ is the length of the inlet, $U$ is the average velocity at the inflow

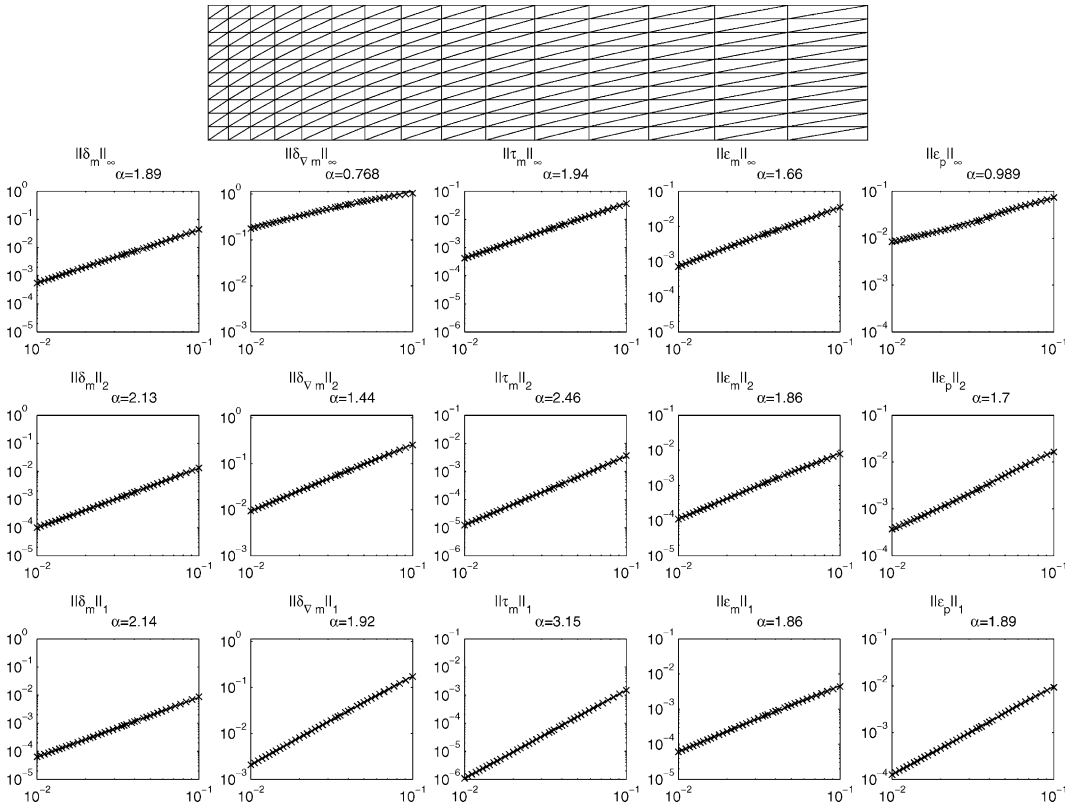


Fig. 11. Accuracy of the computed Kovasznay flow – stretched Courant grid.

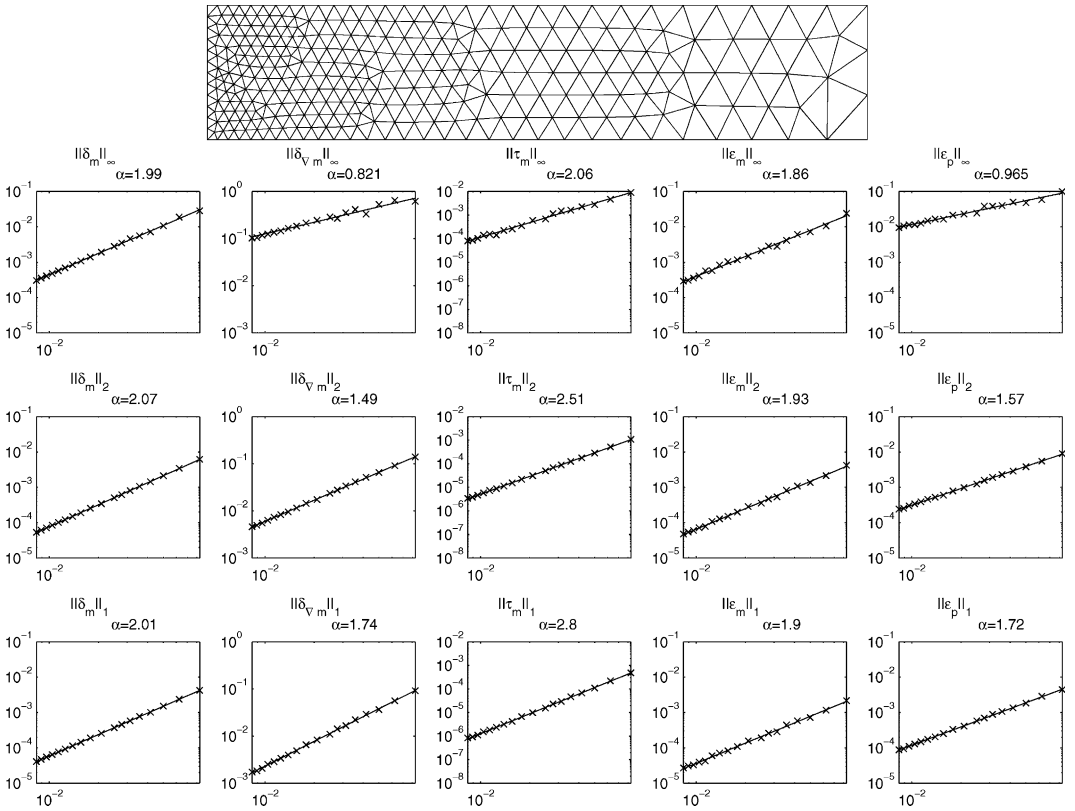


Fig. 12. Accuracy of the computed Kovasznay flow – unstructured grid.

boundary for $t \geqslant 1$, $\mu$ is the viscosity and $\rho = 1$ is the density. Fig. 14 shows the stationary solution for $Re = 800$ obtained on a grid consisting of 3320 triangles.

Velocity profiles at distances 7 and 15 from the step obtained for $Re = 800$ with the finest regular grid that we used are given in Figs. 16 and 17, in comparison with the benchmark data published in [14]. The error in vertical velocity in Fig. 16 is not as bad as it seems, because this quantity is close to zero.

We calculated the position of the reattachment point as a function of a mesh parameter, and compared it to the experimental data published in [15] and to the numerical prediction of [16]. Results are given in Fig. 18. For Reynolds number 400 our scheme gives a very good estimate of this parameter, which is known to be very sensitive to numerical dissipation.

Reynolds number 800 is very high for an upwind-biased scheme, because the influence of artificial viscosity becomes considerable. There is a noticeable discrepancy between the experimental results [15] and the numerical prediction [16]. For a coarse grid the reattachment point computed by our method is way off. However, Fig. 18 shows that for fine grids our method gives a more accurate prediction than [16].

### 6.3. Flow around a circular cylinder

Flow past a circular cylinder is a classical example of an unsteady flow. For $\mathrm{Re} > 47$ vortex shedding occurs, and Karman street of vortices is formed in the wake of the cylinder. Schemes with too much artificial viscosity show onset of unsteadiness at higher Re, or not at all. For higher Reynolds number flow

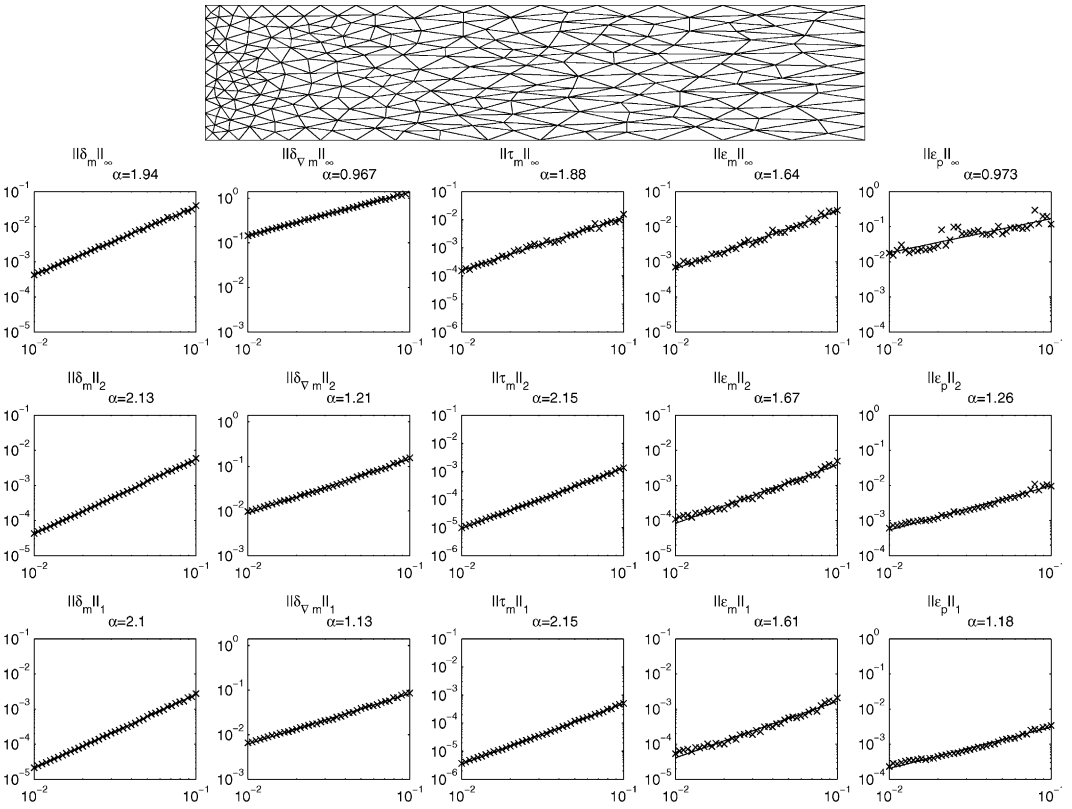


Fig. 13. Accuracy of the computed Kovasznay flow – stretched unstructured grid.

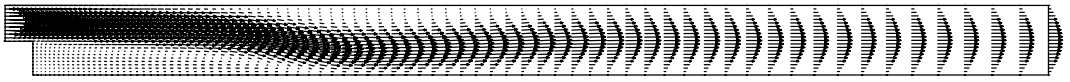

Fig. 14. Backward facing step, $Re = 800$.

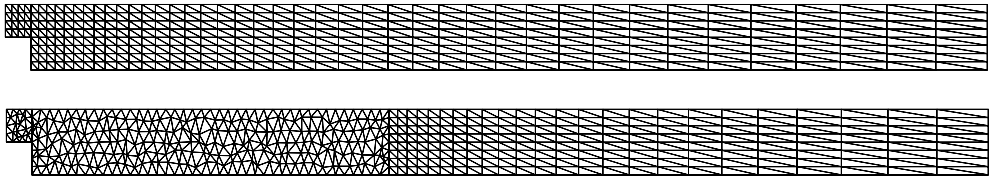

Fig. 15. Grids used for the backward facing step problem. Upper: "regular", lower: "distorted".

becomes turbulent (see [17]). This shedding process is periodic in time. The dimensionless frequency is called the Strouhal number, defined as $S = D/(uT)$, with $D$ the cylinder diameter, $u$ the upstream velocity and $T$ the period. Williamson and Brown in [17] give the following relation:

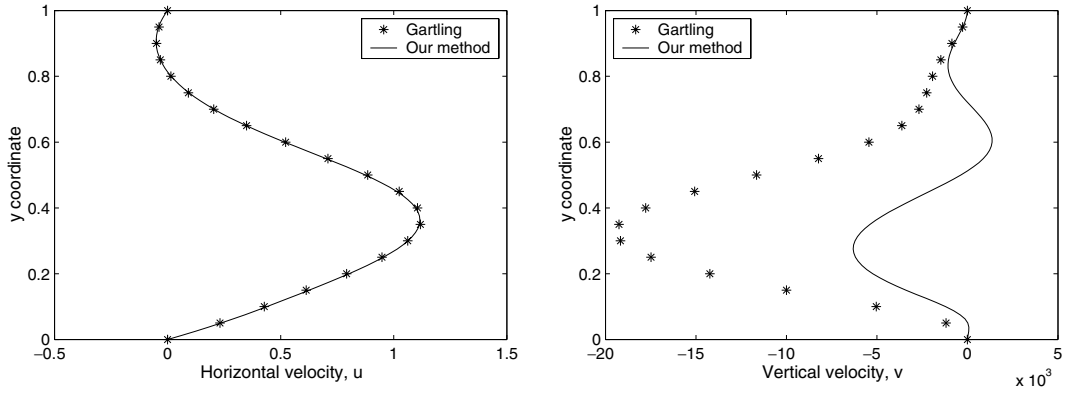


Fig. 16. Velocity profiles at distance 7 from the step.

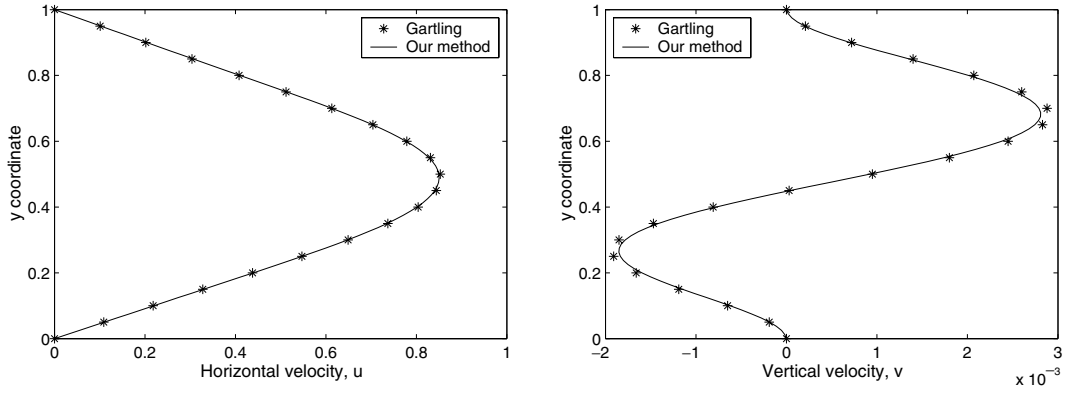


Fig. 17. Velocity profiles at distance 15 from the step.

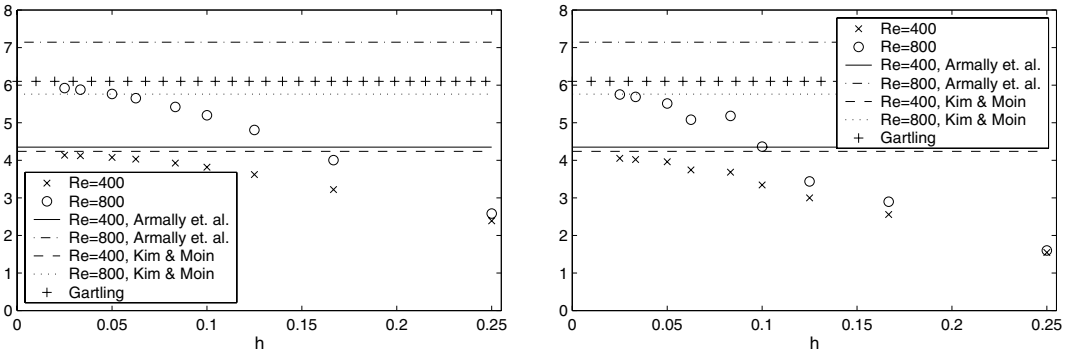


Fig. 18. Position of the reattachment point for regular (left) and distorted grids (right).

$$S = 0.2665 - \frac{1.018}{\sqrt{Re}}, \quad \mathrm{Re} = \frac{\rho u D}{\mu}, \tag{57}$$

which is in good agreement with the experimental data.

We solved this problem for various Reynolds numbers on six grids, one of which is shown in Fig. 19, the other has twice as many nodes along each boundary, the third one has twice as many nodes at the cylinder as the second one, and the other three were made by distorting the first three grids (see Fig. 20). An instantaneous pressure distribution for $\mathrm{Re} = 100$ is shown in Fig. 21.

Obtained Strouhal numbers in comparison with formula (57) are given in Fig. 22. Agreement is quite satisfactory on the medium and fine grids, both regular and distorted.

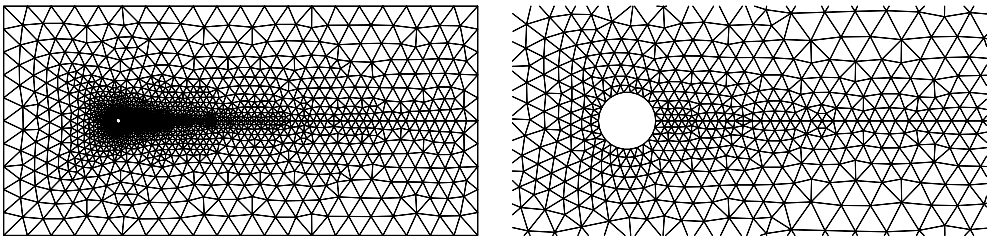

Fig. 19. Regular mesh used for the flow around a cylinder, full (left) and a detail (right).

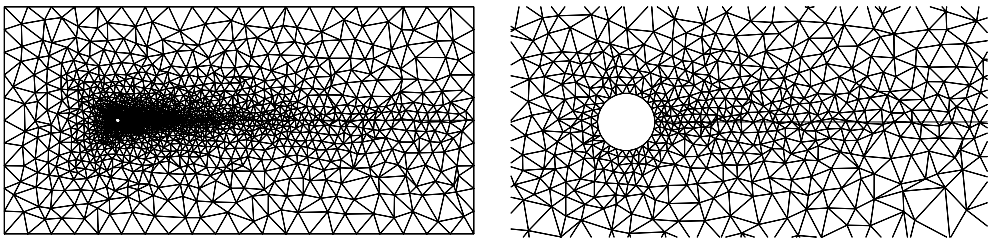

Fig. 20. Distorted mesh used for the flow around a cylinder, full (left) and a detail (right).

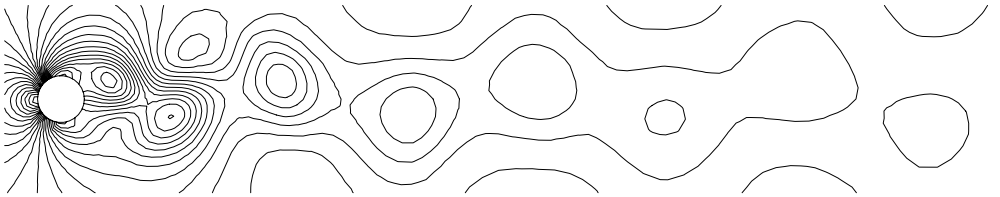

Fig. 21. Pressure distribution in flow around a cylinder.

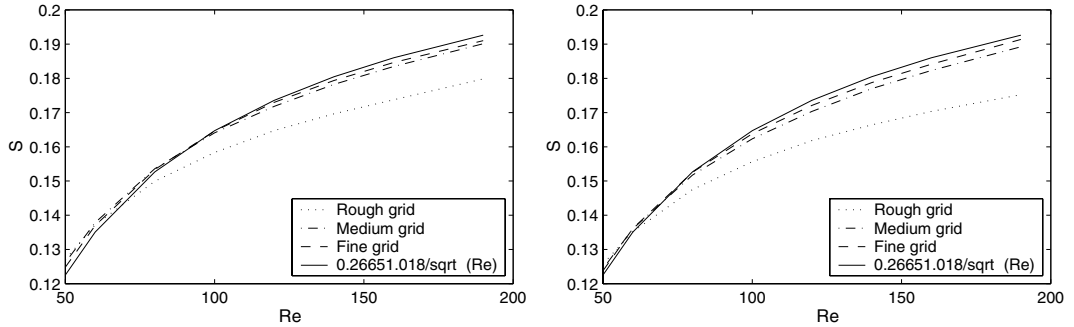


Fig. 22. Strouhal numbers obtained on the regular (left) and the distorted grids (right).

## 7. Possible extensions

### 7.1. Three-dimensional tetrahedral grids

In three dimensions we approximate the momentum field $\vec{m}$ in the vicinity of a mesh node by a linear polynomial equivalent to (10)

$$\vec{m}(\vec{r}) \approx \vec{P}(\vec{r}) = \vec{a} + \vec{b}x + \vec{c}y + \vec{d}z, \quad \vec{a}.\vec{b}, \vec{c}, \vec{d} \in \mathbb{R}^3. \tag{58}$$

This polynomial can be determined from the linear system

$$\vec{N}_e \cdot \vec{P}(\vec{r}_e) = m_e \quad \text{for each face } e \text{ in the reconstruction stencil.} \tag{59}$$

The term *faces* refers to the two-dimensional surfaces of the cells (triangles), and *edges* are line segments connecting the nodes. Vector $\vec{N}_e$ is one of the two possible unit normal vectors in face $e$, and normal momentum $m_e$ is actually the average of the momentum component $\vec{N}_e \cdot \vec{m}$ over triangle $e$.

In the same manner as in the one dimensional case, we integrate the divergence of this polynomial over some tetrahedron $\Theta$ and apply the divergence theorem

$$b_1 + c_2 + d_3 = \nabla \cdot \vec{P} = \frac{1}{|\Theta|} \int \nabla \cdot \vec{P} \mathrm{d}\Theta = \frac{1}{|\Theta|} \sum_e m_e |\Omega_e|, \tag{60}$$

where $\Omega_e$ are the faces of the tetrahedron. If the momentum is prescribed in all faces of one tetrahedron, the divergence of the linear polynomial is determined. Therefore, if the faces of more than one tetrahedron are included in the reconstruction stencil, the rank of the system (59) may be reduced.

To prevent the rank reduction due to the divergence theorem we base the polynomial in a node and try include only the faces that meet in this node in the reconstruction stencil. We reconstruct only the divergence-free part $\overline{\vec{P}}$ of the linear polynomial $\vec{P}$:

$$\overline{P}_1 = P_1, \quad \overline{P}_2 = P_2, \quad \overline{P}_3 = P_3 + (d - b_1 - c_2 - d_3)z. \tag{61}$$

There are only 11 free parameters left.

In the interior points of typical tetrahedral meshes the number of faces meeting in a node is usually around 30. This is clearly more then enough to determine the divergence free polynomial. Of course, as in the two dimensional case, additional rank reduction may occur.

### 7.2. Non-triangular and non-tetrahedral grids

It is highly desirable that a divergence-free polynomial can be determined from the faces meeting in one node only. Since only four faces meet in each internal node of a quadrilateral grid, they do not determine a divergence-free linear polynomial. For the application of our scheme it is therefore advisable to convert a quadrilateral or a mixed-element grid into a triangular grid by subdividing each non-triangular polygon into triangles.

There are 12 faces that meet in each internal node of a three-dimensional rectangular grid. They all belong to three mutually orthogonal planes, four faces in each plane. Restriction of a normal component of a linear polynomial to one of these planes is a scalar linear function of a two-dimensional argument, and therefore it has three free parameters. Since there are four conditions imposed to this linear function, one for each face, equations for these four faces must be linearly dependent. This means that the rank of the related linear system will be at most 9, and a divergence-free linear polynomial cannot be determined. As in the two-dimensional case, to avoid stencil enlargement it is best to divide non-tetrahedral polyhedra into tetrahedra.

## 8. Conclusion

We have elucidated difficulties that arise from polynomial reconstruction of staggered representations of vector fields, and proposed a divergence-free linear reconstruction method that is robust and accurate.

A staggered scheme on unstructured grids for incompressible flows with superlinear convergence has been presented. This scheme employs the proposed reconstruction technique. Our reconstruction method can also be used to improve the order of accuracy of other staggered schemes, which, as noted in [6], is at present generally first-order.

## References

[1] F. Harlow, J. Welch, Numerical calculation of time-dependent viscous incompressible flow of fluid with a free surface, Phys. Fluids 8 (1965) 2182–2189.
[2] C. Hall, J. Cavendish, W. Frey, The dual variable method for solving fluid flow difference equations on Delaunay triangulations, Comput. Fluids 20 (1991) 145–164.
[3] C. Hall, T. Porsching, P. Hu, Covolume-dual variable method for thermally expandable flow on unstructured triangular grids, Int. J. Comput. Fluid Dyn. 2 (1994) 111–139.
[4] R. Nicolaides, T. Porsching, C. Hall, Covolume methods in computational fluid dynamics, in: M. Hafez, K. Oshima (Eds.), Computational Fluid Dynamics Review 1995, Wiley, Chichester, UK, 1995, pp. 279–299.
[5] R. Nicolaides, The covolume approach to computing incompressible flows, in: M. Gunzburger, R. Nicolaides (Eds.), Incompressible Computational Fluid Dynamics, Cambridge University Press, Cambridge, UK, 1993, pp. 295–333.
[6] B. Perot, Conservation properties of unstructured staggered mesh schemes, J. Comput. Phys. 159 (2000) 58–89.
[7] S. Rida, F. McKenty, F. Meng, M. Reggio, A staggered control volume scheme for unstructured triangular grids, Int. J. Numer. Methods Fluids 25 (1997) 697–717.
[8] I. Wenneker, A. Segal, P. Wesseling, A Mach-uniform unstructured staggered grid method, Int. J. Numer. Methods Fluids 40 (2002) 1209–1235.
[9] I. Wenneker, A. Segal, P. Wesseling, Conservation properties of a new unstructured staggered scheme, Comput. Fluids 32 (2003) 139–147.
[10] T.J. Barth, Aspects of unstructured grids and finite-volume solvers for the Euler and Navier–Stokes equations, in: Proc. of the 25th Computational Fluid Dynamics Lecture Series, Von Karman Institute, 1994.
[11] M. Shashkov, B. Swartz, B. Wendroff, Local reconstruction of a vector field from its normal components on the faces of grid cells, J. Comput. Phys. 139 (1998) 406–409.
[12] P. van Beek, R. van Nooyen, P. Wesseling, Accurate discretization on non-uniform curvilinear staggered grids, J. Comput. Phys. 117 (1995) 364–367.
[13] L. Kovasznay, Laminar flow behind a two-dimensional grid, Proc. Cambridge Philos. Soc. 44 (1948).
[14] D. Gartling, A test problem for outflow boundary conditions – flow over a backward facing step, Int. J. Numer. Methods Fluids 11 (1990) 953–967.
[15] B. Armaly, F. Durst, J. Pereira, B. Schönung, Experimental and theoretical investigation of backward-facing step flow, J. Fluid Mech. 127 (1983) 473–496.
[16] J. Kim, P. Moin, Application of a fractional-step method to incompressible Navier–Stokes equations, J. Comput. Phys. 59 (1985) 308–323.
[17] C. Williamson, G. Brown, A series in $1/\sqrt{Re}$ to represent the Strouhal–Reynolds number relationship of the cylinder wake, J. Fluids Struct. 12 (1998) 1073–1085.